nature communications

Article

https://doi.org/10.1038/s41467-025-65325-7

Modulating phonon dynamics: tailoring lattice vibrations to enhance thermoelectric efficiency in $Mg_3(Sb, Bi)_2$ alloy

Received: 30 July 2025

Accepted: 11 October 2025

Published online: 24 November 2025

Check for updates

Gang Wu[1], Airan Li[1], Longquan Wang[1], Xinzhi Wu[1], Xinyuan Wang[1,2] & Takao Mori[1,2]

Heat in crystalline materials is transported by phonons from lattice vibrations, and lattice thermal conductivity critically determines thermoelectric performance. Different from conventional approach that reduce thermal conductivity via extrinsic additives sacrificing electrical transport, here, we demonstrate a notable advancement in the n-type $Mg_3Sb_{1.5}Bi_{0.5}$ by modulating phonon dynamics through lattice softening and simultaneously suppressing the phonon mean free path in a more localized manner while remaining compositionally invariant. Originating from Mg vacancies and derivative defects, elevated internal strain degrades bonding rigidity and localize phonons at the lattice-constant level, yielding an ultra-low thermal conductivity of 0.3 $W m^{-1} K^{-1}$, close to the theoretical minimum. This intrinsic strategy, combined with electron concentration optimization, yields a ZT_{max} of 2.06 and an extraordinary ZT_{ave} of 1.58, exceeding state-of-the-art n-type materials. Furthermore, a single-leg generator and two-pair module deliver conversion efficiencies of 12.5% ($\Delta T = 440$ K) and 7.4% ($\Delta T = 300$ K), respectively, highlighting exceptional potential for waste heat recovery.

More than half of the energy from fossil fuels is lost as unusable heat during combustion, especially waste heat in the range of near room temperature to below 500 °C, for which there is currently no effective method to capture and convert this low-grade energy into useful power[1,2]. Thermoelectric (TE) generators could directly convert heat and electricity via the Seebeck effect, thereby efficiently utilizing waste heat and promoting sustainable energy development[3–5]. The crucial factor in enhancing the conversion efficiency (η) of TE generators relies on achieving a high dimensionless figure of merit, $ZT = S^2\sigma T/\kappa_{tot}$, where S, σ, T and κ_{tot} stand for the Seebeck coefficient, electrical conductivity, temperature, and total thermal conductivity, containing electronic (κ_{ele}), lattice (κ_{lat}) and bipolar (κ_{bip}) thermal conductivity, respectively. Realizing a high ZT hinges on a high power factor ($S^2\sigma$) and low thermal conductivity, yet these parameters are coupled together and varied by carrier concentration and mobility[6,7].

It is, in general, difficult to enhance any individual TE parameter without compromising the others[8,9]. Among S, σ, and κ, the κ_{lat} is regarded as the only parameter that can be tuned independently[10,11]. Thermodynamically, the κ_{lat} is basically dominated by the phonon propagation dynamics, quantized lattice vibrations that govern heat transport. Usually, traditional strategies for κ_{lat} regulation predominantly rely on introducing nanostructures, including secondary phases, interfaces, or grain boundaries on the tens to hundreds of nanometer scale to disrupt vibrational coherence, which reduces the phonon mean free path (l) and lowers the κ_{lat}[12,13]. While these structures effectively scatter mid- to low-frequency phonons, their comparable dimensions to carrier mean free paths inevitably deteriorate carrier mobility. According to the phonon gas model[14,15], the κ_{lat} could be

[1]Research Center for Materials Nanoarchitectonics (MANA), National Institute for Materials Science (NIMS), Tsukuba, Japan. [2]Graduate School of Pure and Applied Science, University of Tsukuba, Tsukuba, Japan. e-mail: MORI.Takao@nims.go.jp

expressed as[16]:

$$\kappa_{lat} = \frac{1}{3} C_v v l \quad (1)$$

where C_v, v represent heat capacity and the sound velocity, respectively. Apart from tailoring lattice vibrations through phonon mean free path regulation, the modulation of sound velocity is often overlooked. To minimize κ_{lat}, two synergistic strategies appear. As illustrated in Fig. 1b[12,17–22], it is crucial to simultaneously lessen the product of the mean free path and sound velocity ($v \times l$) in a localized manner, to effectively decouple thermal and electronic transport. When phonon-phonon interactions are the primary scattering mechanism, the phonon gas model formula could also be written as follows[23,24]:

$$\kappa_{lat} = \frac{(6\pi^2)^{\frac{2}{3}} \bar{M}}{V^{\frac{2}{3}} 4\pi^2 \gamma^2} \frac{\left\langle v_g^3 \right\rangle}{T} \quad (2)$$

where V, γ, and $\bar{M}$ symbolize the atomic volume, Grüneisen parameter, and mean atomic weight, respectively. It can be seen that κ_{lat} is more sensitive to lattice bonding stiffness. In other words, reducing the elastic properties, comprising average sound velocity, Shear modulus, Young's modulus, or increasing the Grüneisen parameter and lowering the Debye temperature, weakens the bonding stiffness, which causes lattice softening and loosens up phonon propagation, and minimizes the effect on electron transport due to the defect-dominated charge scattering. This dual strategy, centered on tailoring lattice vibrations locally, reduces the adverse correlation between κ_{lat} and carrier mobility, which is a cornerstone for optimizing TE performance.

Bi_2Te_3 is currently the most widely used TE material[25–28], but its scarce tellurium and poor mechanical properties, especially for its n-type counterpart, have long plagued the industry[29,30]. Ever since Tamaki et al. achieved a high ZT value of 1.5 in n-type $Mg_3(Sb, Bi)_2$ by adding excess Mg content to lower the formation energy of Mg vacancies, $Mg_3(Sb, Bi)_2$ has attracted widespread attention for its high performance, low cost and plasticity[31–42]. Owing to the complex hierarchical structure, $Mg_3(Sb, Bi)_2$ naturally exhibits a low intrinsic lattice thermal conductivity ($\kappa_{lat} \approx 1\,W\,m^{-1}\,K^{-1}$ at room temperature)[43,44], though it is till sizably larger than the theoretical limit. Due to the high vapor pressure of Mg, many strategies have emerged to refine the electrical transport properties. For example, increasing the sintering temperature, synthesizing single crystals and annealing in the Mg atmosphere to boost grain size[45–48], or doping with elements, such as Nd, Mn, and Cu to alter electron scattering mechanisms have all been employed[42,49–53]. These efforts primarily focus on electronic conduction. However, the critical dimension of phonon dynamics modulation through lattice vibrational tailoring remains insufficiently addressed.

In this work, in contrast to the conventional approach that depends on substantial fluctuations in chemical makeup by extrinsic additives to reduce κ_{lat} at the price of electrical properties, we propose an atomic-scale localized defect engineering strategy: constructing sub-nanometer point defects, such as vacancies with associated local strain fields within the lattice, prioritizing atomic-scale phonon scattering while strategically suppressing electronic degradation. Vacancy-induced strain fields are especially pronounced compared to those from extrinsic dopants. Taking n-type $Mg_3(Sb, Bi)_2$-based material as a prototype, its TE properties are known to be highly sensitive to Mg vacancies. However, conventional approaches through crude reduction of initial Mg content fail to precisely control vacancy concentration, with excessive vacancies triggering conductivity type inversion to p-type conduction. To address this, we exploit the characteristic of high saturated vapor pressure of Mg at elevated temperatures, dynamically tuning vacancy concentration via prolonged sintering time. After carrier concentration tunning by MnTe, intrinsic lattice softening amplification coupled with selective phonon mean free path restriction by leveraging conventional sintering techniques, synergistically suppresses phonon propagation. Originating from Mg vacancies and their derivative defects, elevated internal strain degrades bonding rigidity and defects suppress phonon mean free path, resulting in an ultra-low lattice thermal conductivity. The schematic of the main mechanism is shown in Fig. 1a. Although a certain number of dislocations and nanopores are likely to form due to vacancy clustering during prolonged sintering to affect the electrical performance, their impact may further mitigate by the carrier concentration and density of states effective mass decrease. As a result, through fine-tuning the Mg vacancy, the carrier concentration and mobility remain at high levels, maintaining the power factors in the $x = 0.01$ (20 min) sample, and the product of phonon velocity and phonon mean free path decreases to an extremely low value below previous samples[31,51,53–56], displayed in Fig. 1c, lowering the lattice thermal conductivity to $0.3\,W\,m^{-1}\,K^{-1}$, close to the theoretical minimum, achieving a partial decoupling of electrical and thermal transport. Consequently, one of the highest ZT_{max} of 2.06, notable average ZT_{ave} of 1.04 (300–500 K) and extraordinary $ZT_{ave} = 1.58$ (300–723 K) are obtained, showing its competitiveness to any other n-type TE materials near room temperature, and superiority in the mid-temperature region, as shown in Fig. 1d[57–65]. Most importantly, we achieve a high conversion efficiency of 12.5% ($\Delta T = 440$ K) and 7.4% ($\Delta T = 300$ K) for a single TE-leg generator and a two-pair module in Fig. 1e[21,22,29,51,56,58,60,66–71], respectively. Compared to both commercial Bi_2Te_3 modules or other TE systems, the initial conversion efficiency obtained in this work exhibits strong competitiveness, highlighting great potential for waste heat recovery.

Results

Modulating thermal properties by tailoring lattice vibrations, including lattice softening and suppressed phonon mean free path

Firstly, the doped MnTe in $Mg_{3.2}Sb_{1.5}Bi_{0.5}$ is to optimize the carrier concentration. As shown in Fig. S1, the electrical conductivity increases from 219 S cm^{-1} for $x = 0.005$ to 481 S cm^{-1} for $x = 0.02$ sample. The increase in electrical conductivity is primarily due to the rise in carrier concentration following MnTe doping. In addition, with the enhancement of MnTe content, the carrier-scattering mechanism shifts from being dominated by grain boundary scattering to mixed scattering before 400 K, which is beneficial for optimizing TE performance in the room-temperature range. Ultimately, a peak ZT of 1.73 at 723 K is achieved in the $x = 0.01$ sample. So, the subsequent discussion will focus on the $x = 0.01$ composition.

Tailoring lattice vibrations at the local scale is essential to decouple electrical-thermal performance by weakening the adverse correlation between κ_{lat} and carrier mobility. Unlike conventional extrinsic doping methods that rely on substantial fluctuations in chemical composition, we modulate phonon transport locally by creating sub-nanometer point defects, such as vacancies with associated strain fields, that weaken bond stiffness and enhance phonon scattering, while strategically minimizing adverse effects on electron transport. However, excess Mg vacancies are believed to be detrimental to the performance of n-type $Mg_3(Sb, Bi)_2$-based materials. It is critical to reconcile this competing effect and tune the vacancy concentration to an optimal range in order to balance electrical and thermal transport. We adopt an initial composition with slight excess Mg and MnTe compound to ensure robust n-type conductivity with an adequate carrier concentration. Exploiting the characteristic of high saturated vapor pressure of Mg at elevated temperatures, Mg vacancies are dynamically tuning by extending the sintering time to achieve balanced TE transport, which is further discussed later. To further demonstrate the necessity of such fine Mg vacancy regulation, we also prepare samples with different initial Mg contents to investigate the effect of starting composition as shown in Fig. S2. These results show

https://doi.org/10.1038/s41467-025-65325-7

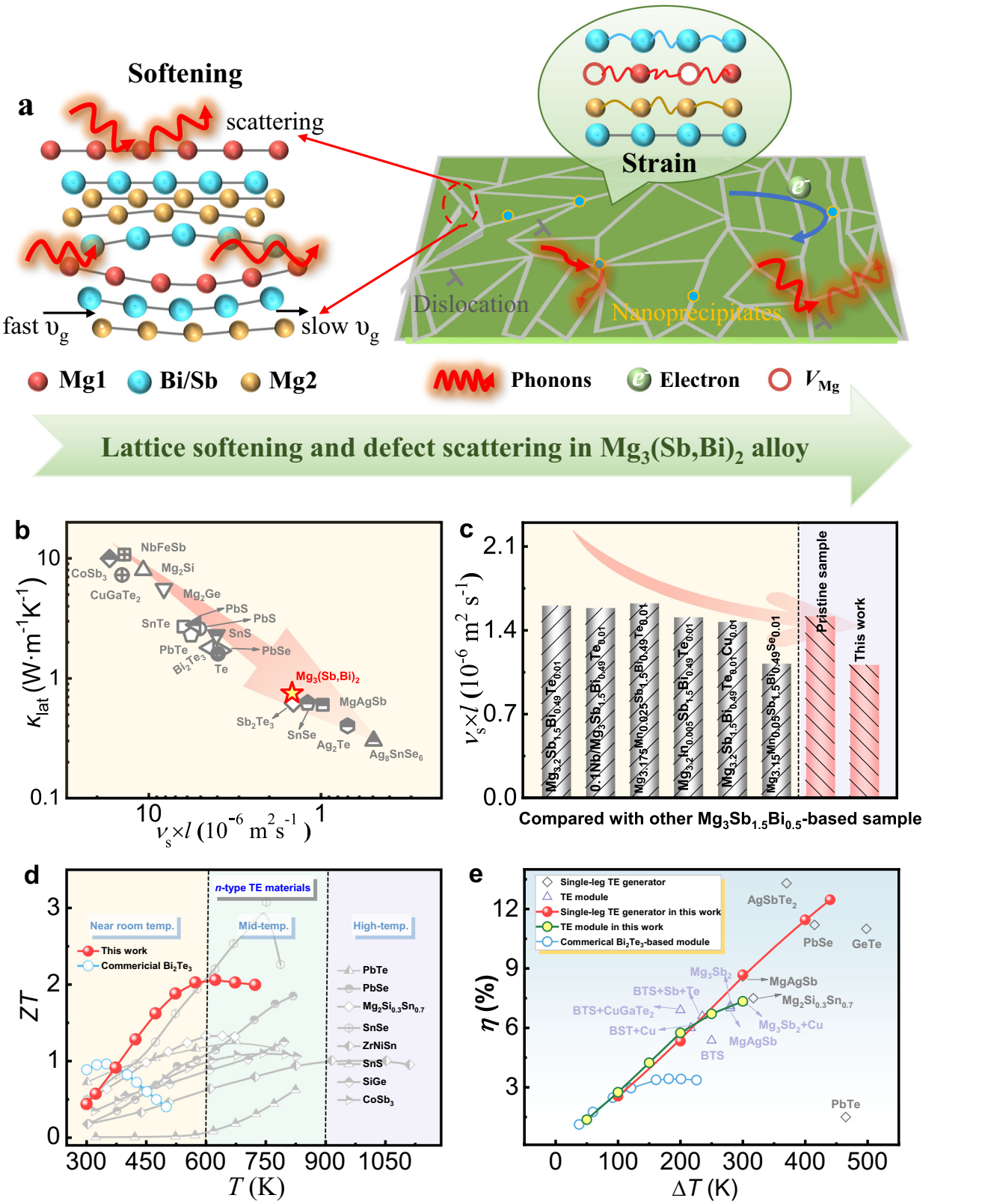

Fig. 1 | Lattice softening and defects enhances phonon scattering and enables superior thermoelectric (TE) performance in $Mg_3(Sb, Bi)_2$-based alloys. **a** Schematic diagram of the lattice softening and phonon scattering mechanism in the $Mg_3(Sb, Bi)_2$-based alloy. **b** $\upsilon \times l$ *vs.* κ_{lat} at 300 K for various TE systems. **c** The comparison of $\upsilon \times l$ with other $Mg_3Sb_{1.5}Bi_{0.5}$-based sample. The comparison of (**d**) *ZT* value and **e** conversion efficiency η with other TE systems.

that the conventional approaches through crude reduction of initial Mg content fail to precisely control vacancy concentration.

$Mg_3(Sb, Bi)_2$-based alloys belong to the α-La_2O_3-type structure. As Fig. S3 shows, the X-ray diffraction (XRD) patterns of $(Mg_{3.2}Sb_{1.5}Bi_{0.5})_{1-x}(MnTe)_x$ samples at room temperature are well indexed to the Mg_3Sb_2 structure (JCPDS#03-0375). There is a single-phase structure without any impurity phases within the detection limits of XRD. We have also performed SEM analysis on two representative samples, $x = 0.01$

https://doi.org/10.1038/s41467-025-65325-7

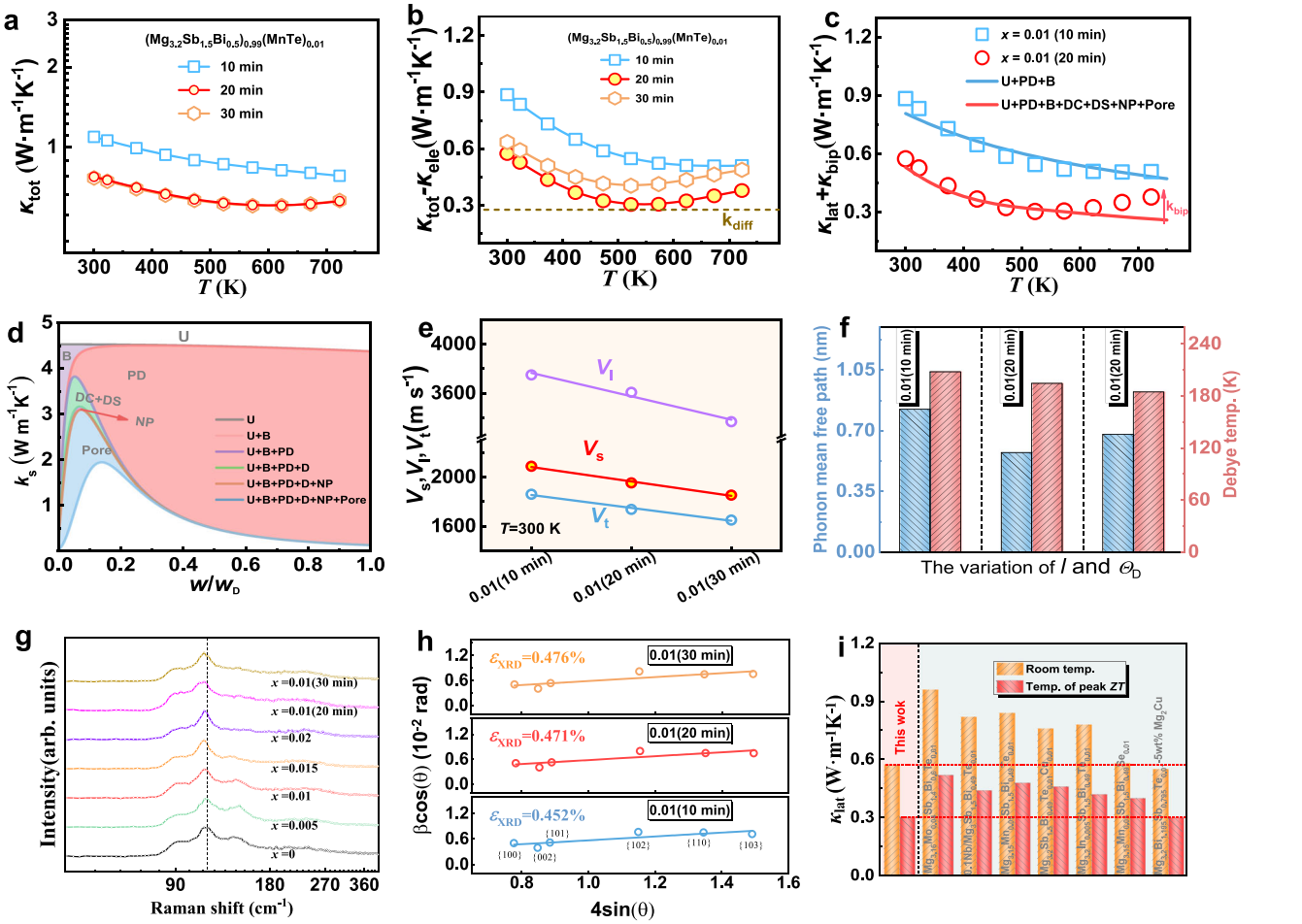

Fig. 2 | Temperature-dependent thermal transport properties and phonon scattering analysis of $(Mg_{3.2}Sb_{1.5}Bi_{0.5})_{0.99}(MnTe)_{0.01}$ samples. The temperature-dependent thermoelectric (TE) properties of $(Mg_{3.2}Sb_{1.5}Bi_{0.5})_{0.99}(MnTe)_{0.01}$ samples at different sintering condition, **a** κ_{tot}, **b** κ_{tot}-κ_{ele}, **c** the sum of κ_{bip} and κ_{lat}. **d** The frequency-dependent κ_s for the $x = 0.01$ (20 min) sample at room temperature on the basis of the Debye–Callaway model. **e** Sound velocities. **f** The comparison of phonon mean free path, Debye temperature. **g** Raman spectrum for the $(Mg_{3.2}Sb_{1.5}Bi_{0.5})_{1-x}(MnTe)_x$ samples at room temperature. **h** The Williamson–Hall strain analysis of $x = 0.01$ (10, 20, 30 min) samples. **i** The comparison of κ_{lat} in this work with those of other reports.

(10 min) and $x = 0.01$ (20 min) shown in Figs. S4 and S5. In both samples, the elemental mapping shows that Mg, Sb, Bi, Mn and Te are homogeneously distributed throughout samples. No obvious segregated MnTe compound is observed. To elucidate phonon transport behavior, the thermal performance parameters are presented in Fig. 2. As shown in Fig. 2a, the κ_{tot} near the room temperature gradually decreases as the sintering holding time is extended. A relatively low κ_{tot} of 0.6 W m^{-1} K^{-1} at 623 K is acquired for the $x = 0.01$ (20 min) sample. The variations in κ_{tot} are associated with fluctuations in κ_{ele}, shown in Fig. S6b, where κ_{ele} is calculated by the Wiedemann–Franz law, $\kappa_{ele} = L\sigma T$, and L is the Lorenz number estimated by the empirical formula[72] $L = 1.5 + \exp(-|S|/116) \times 10^{-8}$ V^2 K^{-2} and plotted in Fig. S6a. The κ_{tot}-κ_{ele}, displayed in Fig. 2b, gradually decreases with rising temperature, while it experiences a slight increase at high temperatures due to the bipolar effect. It is interesting that a lower value of κ_{lat} is acquired after extending the sintering holding time, dropping from 0.88 W m^{-1} K^{-1} for the $x = 0.01$ (10 min) sample to 0.57 W m^{-1} K^{-1} for the $x = 0.01$ (20 min) sample at room temperature, a reduction of over 30%. Notably, the lowest value decreases to 0.3 W m^{-1} K^{-1} at 623 K, which is close to the theoretical minimum predicted by the diffusion limit[73]. The calculation of the theoretical minimum is provided in the Supporting Information. The reason for the diminishment of lattice thermal conductivity is primarily attributed to the phonon mode softening and enhanced phonon scattering, which is further discussed later.

Elastic properties are commonly used to gauge the inter-atomic bonding strength in a crystal lattice. To further scrutinize the reasons behind the reduction in thermal conductivity, we undertake investigation of the elastic properties to estimate the chemical bond strength. The calculation method for the elastic properties is provided in the Supporting Information. As we can see from Fig. 2e, at room temperature, the longitudinal (v_l), transverse (v_t) and mean (v_s) sound velocities decrease obviously when the sintering holding time is extended. Meanwhile, elastic parameters including the Shear and Young's modulus, have also noticeably decreased, as shown in Table S1. The lessened elastic properties suggest a weakening of the chemical bonding stiffness in the $Mg_{3.2}Sb_{1.5}Bi_{0.5}$ material, which commonly engenders lattice softening and impedes phonon propagation. Besides elastic properties, the Debye temperature can also serve as an indicator of atomic bonding strength. As shown in Fig. 2f, the Debye temperature steadily decreases with extended sintering holding time, which aligns with the conclusions derived from the elastic properties. According to the ball-and-spring model by Heremans[74], weaker inter-atomic bonding strength is associated with stronger anharmonicity, and as shown in Table S1, the sample's anharmonicity also increases.

To gain deeper insights into the reduction in elastic properties, we calculate the internal strain of powder samples via XRD. Figure 2h

presents the measurement of internal strain according to the Williamson–Hall function[75], with the calculation details provided in the Supporting Information, and ε represents the magnitude of the internal strain. It is obvious that there exists a significant increase in internal strain with prolonged sintering holding time, which primarily originates from the stress field induced by the higher density of V_{Mg} and their derivative defects, with further discussion later. Typically, defect-induced internal strain fields usually modify phonon frequencies, which in turn leads to lattice softening. Therefore, the lattice softening induced by internal strain leads to a reduction in thermal conductivity. The peak positions of the Raman spectrum for samples at room temperature gradually shift to the lower frequency area, shown in Fig. 2g, indicating the lattice softening as well. By the way, the phonon mean free path of samples decreases significantly with the extending sintering holding time displayed in Fig. 2f, especially for the $x = 0.01$ (20 min) sample, which is reduced to 0.57 nm and close to the lattice parameters of the unit cell. This indicates that phonon transport has been nearly suppressed to its limit through scattering, contributing to the obtained extremely low lattice thermal conductivity.

To further quantitatively elucidate the effect in the reduction of κ_{lat}, we employ the Debye–Callaway model to theoretically analyse[76]:

$$\kappa_{lat} = \frac{k_B}{2\pi^2 v}\left(\frac{k_B T}{\hbar}\right)\int_0^{\theta_D/T} \tau_{tot}(x)\frac{x^4 e^x}{(e^x-1)^2}dx \quad (3)$$

where $x = \hbar\omega/k_B T$, k_B, $\hbar$, τ_{tot} are the reduced phonon frequency, Boltzmann constant, reduced Plank constant, and phonon relaxation time, respectively. More details and corresponding parameters can be seen in Supporting Information and Table S2. This model primarily considers phonon-phonon Umklapp process (U), grain boundary scattering (B), point defect scattering, dislocations scattering, strain scattering (DS), nanoprecipitates (NP) and nanopores (Pore). As shown in Fig. 2c, the experimental data align well with the theoretical calculations, confirming that lattice softening and defect scattering are the primary reasons for the reduction in lattice thermal conductivity. It can be also observed that the bipolar effect becomes more pronounced with the extending sintering holding time, because of the decrease in carrier concentration. The frequency-dependent κ_s for the $x = 0.01$ (20 min) sample at room temperature is plotted in Fig. 2d. The reduction in lattice thermal conductivity originates from Mg vacancies and their derived defects, which act at different levels. The isolated Mg vacancies contribute at the atomic scale through point-defect scattering. And during prolonged sintering, Mg vacancies tend to aggregate, giving rise to vacancy clusters, dislocations, nanopores[77], that act at larger length scales and further enhance phonon scattering. In this sense, the internal strain generated by Mg vacancies and their derivative defects leads to lattice softening, while these defects suppress the phonon mean free path. Together, they jointly constitute the main origin of the lattice thermal conductivity reduction. Thus, the obtained κ_{lat} is lower than those of most reported values, both at room and the peak ZT temperature, as shown in Fig. 2i[51,53–56,78,79].

We further explore more microstructure analysis to gain insights into phonon transport behavior. A certain of Mg vacancies' derived defects, such as dislocations and nanopores, form due to vacancy clustering during prolonged sintering. Some defects, including obvious dislocations and NP, have found through the low-magnification transmission electron microscopy images plotted in Fig. 3a–c. A certain of nanoscale pores forms from the STEM images in Fig. S7, which have the ability to scatter low- and medium frequency phonons. From the EDS elemental mapping in Fig. 3d, there is a significant Bi-rich aggregation near the grain boundaries, which is also confirmed through line scanning in Fig. S8. The same phenomenon is also observed in other regions of the same sample shown in Fig. S9. These NP have a diameter of nearly tens of nanometers, which often results in the formation of stacking faults and induces internal stress. The high density of lattice distortions, stacking fault and NP can also be noticed in the high-resolution transmission electron microscopy images within the grain and near the grain boundary shown in Fig. 3e, f, which is beneficial to impede phonon propagation. Figure 4g exhibits the strain maps by the geometric phase analysis (GPA) along different directions, inducing large strain fluctuation near the grains, which regularly triggers phonon mode softening. Furthermore, compared with the $x = 0.01$ (10 min) sample, the dislocation density increases by nearly 50% in $x = 0.01$ (20 min) sample from the EBSD analysis seen in Fig. 3h, i. All in all, widespread stress fluctuations and numerous defects are responsible for the lattice softening and phonon scattering, as depicted in the primary phonon scattering mechanisms diagram of Fig. 1a, which results in the obtained ultra-low κ_{lat}, and is consistent with the analysis above. Although the newly introduced dislocation defects also adversely affect electron transport, the reduced carrier concentration and density of states effective mass can mitigate this impact, as discussed later.

In addition, from the SEM images shown in Fig. S10, the number of micron-scale pores increases significantly from $x = 0.01$ (20 min) to $x = 0.01$ (30 min) samples as the sintering time further increases. The gradual decrease in sample density listed in the Table S3 with increasing sintering time also indirectly indicates a corresponding rise in pores. In the geometric-scattering regime, large pores scatter primarily long-wavelength phonons, which contribute partly to reduction of thermal resistance. Therefore, upon further extension to 30 min, the nanoscale pores tend to coarsen and agglomerate into micron-scale pores, resulting in a slight enhancement in the phonon mean free path and κ_{lat} compared to the $x = 0.01$ (20 min) sample shown in Fig. 2b, f.

High electrical transport maintenance and ZT value enhancement

Besides thermal transport, maintaining high electrical performance is also crucial. As shown in Fig. 4a, with extending the sintering holding time, the carrier-scattering mechanism shifts toward grain boundary scattering. And the electrical conductivity deteriorates severely when the sintering holding time extends to 30 min. From the grain size distribution in EBSD images shown in Fig. S11, there is no significant change in the average grain size. So, the carrier-scattering mechanism alteration is attributed to the formation of Mg vacancies during prolonged holding time, which is also supported by the gradual decrease in carrier concentration, as shown in Fig. 4b. From the XRD refinement results shown in Figs. S12–S14 and Table S4, the Mg site occupancy decreased markedly, further confirming an increase in Mg vacancy concentration. Therefore, sustaining high electrical conductivity necessitates an appropriate sintering holding time, further evidencing the existence of a critical Mg vacancy concentration and the imperative for dynamically regulating vacancy concentration to decouple phonon-electron interactions in $Mg_3(Sb, Bi)_2$-based materials. Additionally, with the increase of Mg vacancy concentration, the carrier mobility does not deteriorate due to the reduction in carrier concentration, which mitigates the adverse impact of dislocation defects on carrier scattering.

The temperature-dependent Seebeck coefficient of samples is shown in Fig. 4c. The Seebeck coefficient gradually increases with rising temperature, and the negative values denote a typical n-type conducting behavior. The Seebeck coefficient shows no significant change in $x = 0.01$ (10 min) and $x = 0.01$ (20 min) samples, whereas $x = 0.01$ (30 min) sample exhibits a marked increase, primarily due to the reduction in carrier concentration. The curve between carrier concentration and Seebeck coefficient is plotted in Fig. 4d to further consider the electronic transport properties on the basis of single parabolic band model. In samples with extended sintering holding time, the density of states effective mass decreases partially. We have performed EPMA compositional analysis on samples with different holding times. As we can see from Figs. S15–S17 and Table S5, all

https://doi.org/10.1038/s41467-025-65325-7

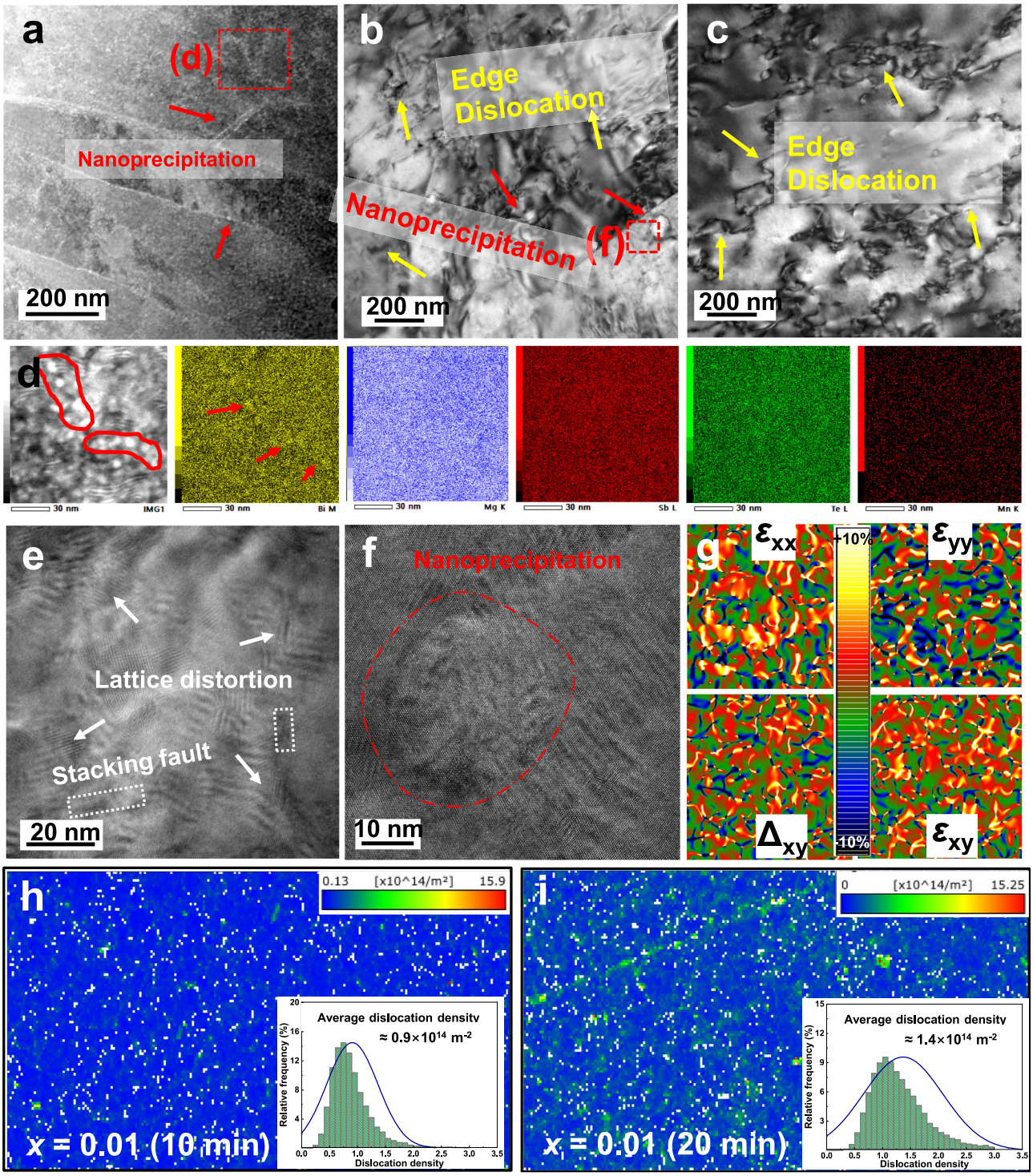

Fig. 3 | The microstructure analysis of $x = 0.01$ (20 min) sample by STEM. a–c the different microstructure images showing a high density of lattice defects, and the defects indicated by the yellow arrows corresponding to dislocations, while those marked by the red arrows representing nanoprecipitates. **d** The EDS elemental mapping of Mg, Bi, Sb, Mn and Te along the grain boundary. **e**, **f** High-magnification STEM micrograph of lattice distortions, stacking fault and nanoprecipitates. **g** Strain mapping in (**e**) along different directions is confirmed by the geometric phase analysis (GPA). **h**, **i** The dislocation density distribution of $x = 0.01$ (10 min) and $x = 0.01$ (20 min) samples from EBSD analysis.

elements are homogeneously distributed, and no MnTe compound is observed. By the way, a slight decrease in Mg content is detected as the holding time enhancement, indicating an increased concentration of Mg vacancies. This phenomenon is consistent with the decrease of electron concentration. The observed decrease of the density of states effective mass can be related to the formation of Mg vacancies. A lower electron concentration shifts the Fermi level downward, away from the regions of higher density of states, thereby reducing the effective mass. Some similar phenomena have also been reported in previous studies[54]. The reduction in density-of-states effective mass can also mitigate the effect of carrier mobility by defect-induced electron scattering.

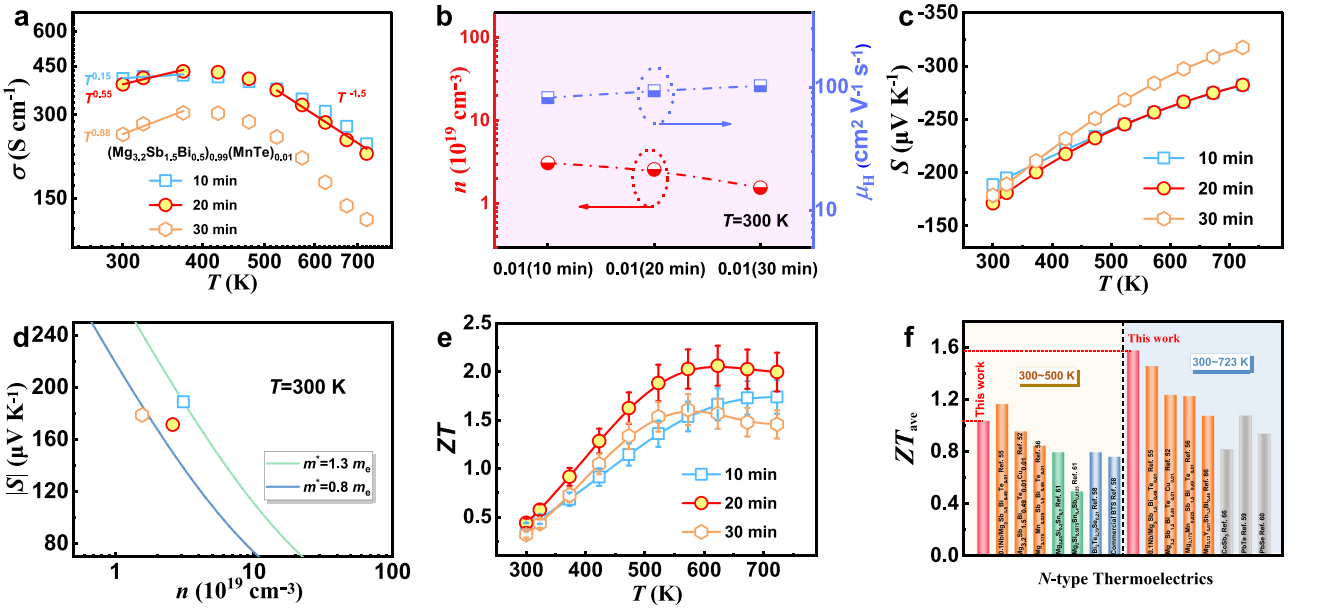

Fig. 4 | The temperature-dependent TE properties of $(Mg_{3.2}Sb_{1.5}Bi_{0.5})_{0.99}(MnTe)_{0.01}$ samples at different sintering condition. a The electrical conductivity, **b** the carrier concentration (n) and carrier mobility (μ) at 300 K. **c** The Seebeck coefficient. **d** The relationship between carrier concentration and Seebeck coefficient on the basis of single parabolic band model. **e** The ZT value. **f** The comparison of the average ZT with other n-type thermoelectric materials at the range of 300–500 K and 300–723 K[51,54,55,57–60,65,85]. Error bars represent ±10% standard deviation relative to the ZT value.

As a result, one of the highest ZT value of 2.06 has been achieved at 623 K, as shown in Fig. 4e. Interestingly, the ZT curve quickly reaches its peak and then gradually levels off, which is very beneficial behavior for obtaining a high average ZT value. This temperature dependence is mainly attributed to the fact that as the temperature increases past the optimum performance, i.e., peak ZT, the enhanced carrier mobility scattering slightly weakens the improvement in electrical transport, while the lattice thermal conductivity in this work, already achieving values close to its theoretical limit, exhibits a relatively small decrease with temperature. Excitingly, the ZT_{ave} reaches 1.04 and 1.58 within the temperature range of 300–500 and 300–723 K shown in Fig. 4f, respectively. In comparison with previous reports on $Mg_3(Sb, Bi)_2$, or any other known n-type TEs, the ZT_{ave} in this work is at the state-of-the-art level and higher than that of commercial Bi_2Te_3. This indicates that the n-type $Mg_3(Sb, Bi)_2$ obtained in this work exhibits significant advantages for waste heat recovery across both the near-room-temperature and mid-temperature ranges. In addition, we reproduce multiple samples of $x = 0.01$ (20 min) and repeatedly test them, and the consistency of the properties is excellent, as plotted in Figs. S18 and S19.

Design, fabrication and assessment of TE module

Both a single-leg and a two-pair TE device have been designed to better demonstrate the TE performance across different temperature ranges[80–82]. Figure 5a illustrates the structure of the single-leg device. To better harness the excellent TE performance and fully exploit the temperature difference, the finite element simulation is carried out. As shown in Fig. 5b, only the appropriate height and cross-sectional area can yield the maximum TE conversion efficiency. Thus, the dimensions of $3.4 \times 3.4 \times 6.5\ mm^3$ have been adopted to fabricate the single-leg device. The contact resistance between the $Mg_3(Sb, Bi)_2$-based leg and the barrier layer is examined using the four-probe method, shown in Fig. S20. The low contact resistance around $10\ \mu\Omega\ cm^2$, plotted in Fig. 5c, indicates a good contact. The slight difference in contact resistances at both ends of the TE leg can be attributed to minor variations in local thermal-mechanical conditions during sintering, but it remains within the typical experimental uncertainty. In addition, the microscopic morphology and element distribution of the interface have been shown in Fig. S21. The elemental distribution is uniform, and there is no apparent elemental diffusion or voids at the interface, consistent with the result of low contact resistance.

As shown in Fig. 5d for the single-leg device, the open-circuit voltage slowly improves with the rising temperature difference. The internal resistance, obtained by the slope of the V–I curve shown in Fig. S22b, increases gradually, primarily due to the decrease in electrical conductivity as the temperature rises. In addition, as the current increases, the output heat flow displayed in Fig. S22a gradually rises due to the enhanced Joule heating and Peltier effect. When the external resistance matches the internal resistance of the device, the output power and conversion efficiency reach their maximum, as shown in Fig. 5e. Ultimately, the maximum conversion efficiency of the single-leg device realizes a conversion efficiency of 12.5% at the 440 K temperature difference, competitive with the highest performance previous reports, as plotted in Fig. 5f[60,78,83–88]. Furthermore, coupled with MgAgSb, the prepared two-pair module after geometrical design, shown in Fig. S23, achieves a high conversion efficiency of 7.4% ($\Delta T = 300$ K). It is indicated that this work has great potential for waste heat recovery, whether in the near-room-temperature or mid-temperature range.

Discussion

In summary, a strategy focusing on modulating phonon dynamics in a more localized manner for minimizing the lattice thermal conductivity without deterioration of electrical transport and thus promoting TEs is proposed. Particularly, in the n-type $Mg_3Sb_{1.5}Bi_{0.5}$-based alloy, lattice vibrations are tailored via dynamically regulating Mg vacancy, pronounced internal strain, and defect proliferation, which soften interatomic bond stiffness and confine phonon propagation to distances comparable to the lattice parameter. These achieve an ultra-low lattice thermal conductivity of $0.3\ W\ m^{-1}\ K^{-1}$, which is close to the theoretical minimum. As a result, one of the highest ZT_{max} of 2.06, ZT_{ave} of 1.04 (300–500 K) and unprecedented 1.58 (300–723 K) are obtained, which achieves a significant competitive edge in the low-to-mid temperature range. Furthermore, as an initial demonstration of

https://doi.org/10.1038/s41467-025-65325-7

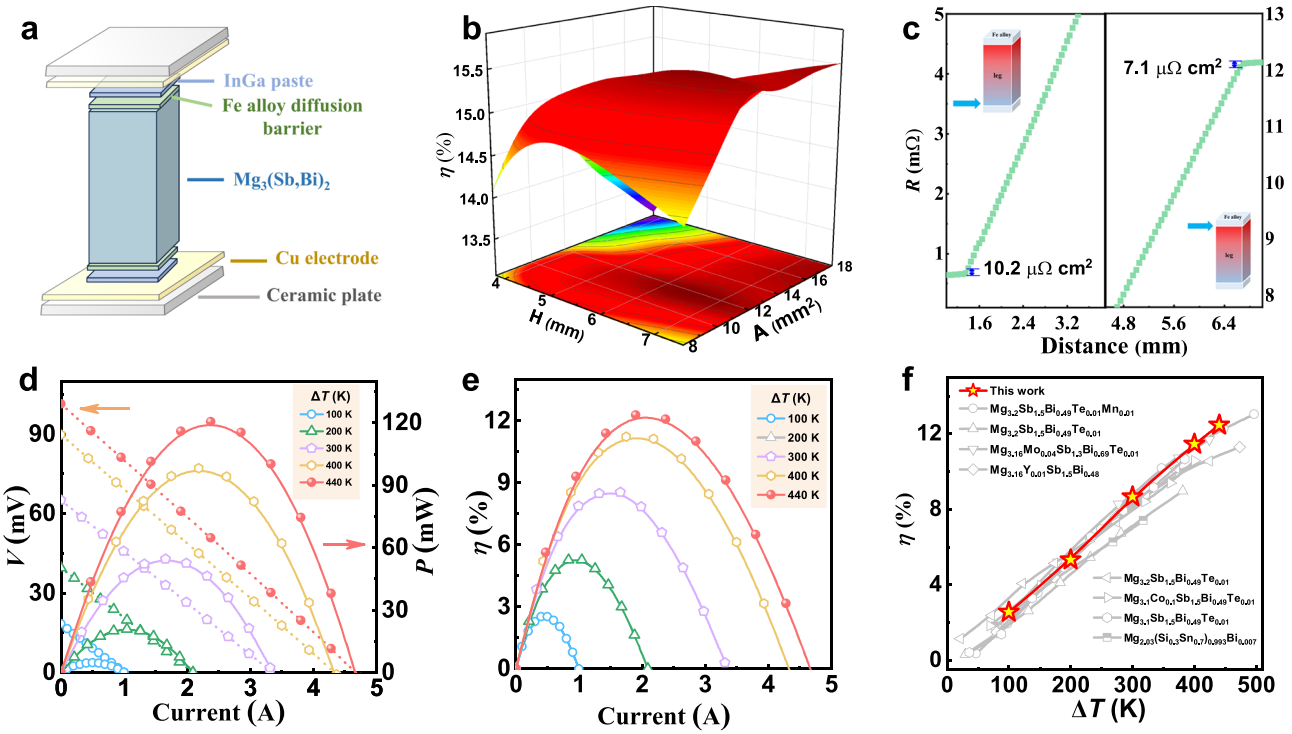

Fig. 5 | The performance of the single-leg thermoelectric device. a Schematic diagram of the single-leg device. **b** The theoretical η as a function of TE leg height and cross-sectional area under the temperature difference of 440 K. **c** The measured contact resistance. The data of single-leg device by current dependence **d** output voltage (V) and output power (P), and **e** the η under the different temperatures. **f** The comparison of η_{max} between the constructed single-leg device in this work and previous reports.

the potential of the material, an excellent conversion efficiency of 12.5% ($\Delta T = 440$ K) and 7.4% ($\Delta T = 300$ K) for a single TE-leg generator and a two-pair module is achieved, respectively. Our work demonstrates the great potential for waste heat recovery of the $Mg_3Sb_{1.5}Bi_{0.5}$-based alloy, whether in the near-room-temperature or mid-temperature range, and demonstration of enhanced lattice vibrations control can enable advancements across various thermal functional materials.

Methods

Sample synthesis

High-purity raw Mg (4N), Bi (4N), Sb (4N) and MnTe (3N) were weighed according to the ratio of $(Mg_{3.2}Sb_{1.5}Bi_{0.5})_{1-x}(MnTe)_x$ ($x = 0$, 0.005, 0.01, 0.015, 0.02). The elements were loaded into the ball milling jar inside an Ar-filled glovebox with an O_2 concentration below 0.1 ppm and then ball-milled (SPEX-Sample Prep 8000 Mixer Mill) for 5 h. The obtained powders were loaded into a φ10 mm graphite die inside the glovebox. It was then immediately sintered using SPS (SPS-1080 System, SPS SYNTEX INC) at 700 °C under 60 MPa for 10, 20, and 30 min.

Measurement and characterization

The electrical conductivity and Seebeck coefficient of all samples were simultaneously measured using ZEM-3 under the He atmosphere. The thermal conductivity was estimated through $\kappa_{tot} = D\rho C_p$, where thermal diffusivity (D) was measured by Netzsch LFA 467, the density of samples (ρ) was calculated by the Archimedes method, and the specific heat capacity (C_p) was determined by the formula $C_p = 3NR(1 + 1.3 \times 10^{-4}\, T - 4 \times 10^3\, T^{-2})/M$[89]. The room temperature electron carrier concentration (n) was measured by the physical properties measurement system, Quantum Design based on the formula $n = 1/R_H e$ and $\mu = \sigma R_H$.

The samples' phase structure was identified by the XRD (SmartLab3, Rigaku) with Cu K_α radiation. The microstructure of samples was characterized using electron backscatter diffraction (EBSD, JSM-7001F, JEOL Inc.), scanning electron microscope (SEM, Hitachi SU4800) fitted with an energy-dispersive spectroscopy (EDS, Horiba EMAXE volution X-Max) and electron probe micro analysis (EPMA, JXA-8500F). The Raman spectroscopy was performed with the 532 nm excitation laser (inVia, Renishaw). The finer microstructure was characterized by scanning transmission electron microscopy (STEM, JEM-ARM-200F-B). The room temperature sound velocity was measured by the Model UVM-2 (Ultrasonic Engineering Co., Ltd).

TE module fabrication and stimulation method

To fabricate the single-leg generator, the sandwiched structure of $(Mg_{3.2}Sb_{1.5}Bi_{0.5})_{0.99}(MnTe)_{0.01}$ powder and Fe alloy (304 stainless steel) powder was employed, using the one-step sintering process. The obtained ingot was cut into dice with dimensions of $3.4 \times 3.4 \times 6.5$ mm^3. The two-pair TE module was fabricated on the basis of n-type $(Mg_{3.2}Sb_{1.5}Bi_{0.5})_{0.99}(MnTe)_{0.01}$ leg with the height of 5 mm and cross-section of 12.25 mm^2, and p-type MgAgSb leg with the height of 5 mm and cross-section of 10.89 mm^2. The MgAgSb leg preparation process can be seen from previous work[22]. The TE module conversion efficiency (η) was measured by Mini-PEM, (ADVANCE RIKO, Japan)[90]. The details of the TE module test and numerical modeling are provided in the Supporting Information.

The numerical simulation of power generation was performed with COMSOL Multiphysics software, version 6.1. The Heat Transfer Module and the Electric Currents Module were coupled through the TE Effect multiphysics interface to simulate the coupled temperature and electrical potential fields. A three-dimensional model was built in the software interface to represent TE legs with a similar geometry and dimension. The temperature-dependent electrical conductivity,

Seebeck coefficient, and thermal conductivity were taken from actual measurement results. Herein, the electrical and thermal contact resistances between interfaces were not considered in our simulation model. The material domains were discretized using a physics-controlled mesh, with the element size set to the default (normal) setting, and a fixed temperature difference was applied between the hot and cold ends.

Statistical analysis

The electronic and thermal transport measurements are independent of sample dimensions, and the uncertainties mainly reflect the instrumental deviations. In particular, the systematic errors are approximately 3% for the Seebeck coefficient and 5% for the electrical conductivity. For the total thermal conductivity, the uncertainty is about 7% calculated from $\frac{d\kappa tot}{\kappa tot} = \sqrt{\left(\frac{d\rho}{\rho}\right)^2 + \left(\frac{dC_p}{C_p}\right)^2 + \left(\frac{dD}{D}\right)^2}$ (1% for the density ρ, 5% for the specific heat C_p and 5% for the thermal diffusion D). Consequently, the propagated error for the calculated ZT values is estimated to be approximately 10%. The computational formula involved is $\frac{d(ZT)}{ZT} = \sqrt{\left(2 \times \frac{dS}{S}\right)^2 + \left(\frac{d\sigma}{\sigma}\right)^2 + \left(\frac{d\kappa tot}{\kappa tot}\right)^2}$.

Reporting summary

Further information on research design is available in the Nature Portfolio Reporting Summary linked to this article.

Data availability

All data generated or analyzed during this study are included in this published article (and its Supplementary Information file).

References

1. Bell, L. E. Cooling, heating, generating power, and recovering waste heat with thermoelectric systems. *Science* **321**, 1457–1461 (2008).
2. Petsagkourakis, I. et al. Thermoelectric materials and applications for energy harvesting power generation. *Sci. Technol. Adv. Mater.* **19**, 836–862 (2018).
3. Snyder, G. J. & Toberer, E. S. Complex thermoelectric materials. *Nat. Mater.* **7**, 105–114 (2008).
4. Yan, Q. & Kanatzidis, M. G. High-performance thermoelectrics and challenges for practical devices. *Nat. Mater.* **21**, 503–513 (2022).
5. Hendricks, T., Caillat, T. & Mori, T. Keynote review of latest advances in thermoelectric generation materials, devices, and technologies 2022. *Energies* **15**, 2022 (2022).
6. Shi, X. L., Zou, J. & Chen, Z. G. Advanced thermoelectric design: from materials and structures to devices. *Chem. Rev.* **120**, 7399–7515 (2020).
7. Zhu, T. et al. Compromise and synergy in high-efficiency thermoelectric materials. *Adv. Mater.* **29**, 1605884 (2017).
8. Mao, J. et al. Advances in thermoelectrics. *Adv. Phys.* **67**, 69–147 (2018).
9. Mori, T. Novel principles and nanostructuring methods for enhanced thermoelectrics. *Small* **13**, 1702013 (2017).
10. Zheng, Y. et al. Defect engineering in thermoelectric materials: what have we learned?. *Chem. Soc. Rev.* **50**, 9022–9054 (2021).
11. Wu, C. et al. Defect engineering advances thermoelectric materials. *ACS Nano* **18**, 31660–31712 (2024).
12. Xiao, Y. et al. Origin of low thermal conductivity in SnSe. *Phys. Rev. B* **94**, 125203 (2016).
13. Wei, P. C. et al. Thermodynamic routes to ultralow thermal conductivity and high thermoelectric performance. *Adv. Mater.* **32**, e1906457 (2020).
14. Morelli, D. T., Jovovic, V. & Heremans, J. P. Intrinsically minimal thermal conductivity in cubic I-V-VI_2 semiconductors. *Phys. Rev. Lett.* **101**, 035901 (2008).
15. Skoug, E. J. & Morelli, D. T. Role of lone-pair electrons in producing minimum thermal conductivity in nitrogen-group chalcogenide compounds. *Phys. Rev. Lett.* **107**, 235901 (2011).
16. Peierls, R. E. & Roberts, L. D. Quantum theory of solids. *Phys. Today* **9**, 29–29 (1956).
17. Guo, Z. et al. A high-efficiency GeTe-based thermoelectric module for low-grade heat recovery. *J. Mater. Chem. A* **10**, 7677–7683 (2022).
18. Zhou, Z. Z. et al. Abnormally low lattice thermal conductivity in ABX honeycomb compounds. *Phys. Rev. Appl.* **16**, 064034 (2021).
19. Xie, L. et al. Realizing excellent thermoelectric performance of Sb2Te3 based segmented leg with a wide temperature range using one-step sintering. *Adv. Electron. Mater.* **6**, 1901178 (2019).
20. Sun, J., Zhang, Y., Fan, Y., Tang, X. & Tan, G. Strategies for boosting thermoelectric performance of PbSe: a review. *Chem. Eng. J.* **431**, 133699 (2022).
21. Zhang, Y. et al. Defect-engineering-stabilized $AgSbTe_2$ with high thermoelectric performance. *Adv. Mater.* **35**, e2208994 (2023).
22. Li, A., Wang, L., Li, J. & Mori, T. Global softening to manipulate sound velocity for reliable high-performance MgAgSb thermoelectrics. *Energy Environ. Sci.* **17**, 8810–8819 (2024).
23. Toberer, E. S., Zevalkink, A. & Snyder, G. J. Phonon engineering through crystal chemistry. *J. Mater. Chem.* **21**, 15843 (2011).
24. Hanus, R. et al. Lattice softening significantly reduces thermal conductivity and leads to high thermoelectric efficiency. *Adv. Mater.* **31**, e1900108 (2019).
25. Wang, X. et al. Enhanced cryogenic thermoelectric cooling of $Bi_{0.5}Sb_{1.5}Te_3$ by carrier optimization. *InfoMat*, **7**, e12663 (2025).
26. Poudel, B. et al. High-thermoelectric performance of nanostructured bismuth antimony telluride bulk alloys. *Science* **320**, 634–638 (2008).
27. Kim, S. I. et al. Thermoelectrics. Dense dislocation arrays embedded in grain boundaries for high-performance bulk thermoelectrics. *Science* **348**, 109–114 (2015).
28. Deng, T. et al. Room-temperature exceptional plasticity in defective Bi_2Te_3-based bulk thermoelectric crystals. *Science* **386**, 1112–1117 (2024).
29. Wu, G. et al. Bi_2Te_3-based thermoelectric modules for efficient and reliable low-grade heat recovery. *Adv. Mater.* **36**, e2400285 (2024).
30. Peng, J. et al. Lattice plainification and intercalation advances power generation and thermoelectric cooling in *n*-type $Bi_2(Te, Se)_3$. *Adv. Energy Mater.* **15**, 2404653 (2025).
31. Tamaki, H., Sato, H. K. & Kanno, T. Isotropic conduction network and defect chemistry in Mg_3Sb_2-based layered Zintl compounds with high thermoelectric performance. *Adv. Mater.* **28**, 10182–10187 (2016).
32. Mao, J. et al. High thermoelectric cooling performance of n-type Mg_3Bi_2-based materials. *Science* **365**, 495–498 (2019).
33. Zhao, P. et al. Plasticity in single-crystalline Mg_3Bi_2 thermoelectric material. *Nature* **631**, 777–782 (2024).
34. Shang, H. et al. N-Type $Mg_3Sb_{2-x}Bi_x$ alloys as promising thermoelectric materials. *Res. (Wash. D. C.)* **2020**, 1219461 (2020).
35. Tang, J., Theja, V. C. S., Liu, K., Karthikeyan, V. & Chen, Y. Advances in Mg_3Bi_2 thermoelectric materials and devices. *Nanoscale* **17**, 53–64 (2024).
36. Shi, X., Wang, X., Li, W. & Pei, Y. Advances in thermoelectric Mg_3Sb_2 and Its derivatives. *Small Methods* **2**, 1800022 (2018).
37. Imasato, K., Kang, S. D. & Snyder, G. J. Exceptional thermoelectric performance in $Mg_3Sb_{0.6}Bi_{1.4}$ for low-grade waste heat recovery. *Energy Environ. Sci.* **12**, 965–971 (2019).
38. Yang, J. et al. Next-generation thermoelectric cooling modules based on high-performance $Mg_3(Bi,Sb)_2$ material. *Joule* **6**, 193–204 (2022).

39. Wood, M., Kuo, J. J., Imasato, K. & Snyder, G. J. Improvement of low-temperature zT in a Mg_3Sb_2-Mg_3Bi_2 solid solution via Mg-vapor annealing. *Adv. Mater.* **31**, e1902337 (2019).
40. Li, A. et al. High performance magnesium-based plastic semiconductors for flexible thermoelectrics. *Nat. Commun.* **15**, 5108 (2024).
41. Li, A., Fu, C., Zhao, X. & Zhu, T. High-performance $Mg_3Sb_{2-x}Bi_x$ thermoelectrics: progress and perspective. *Res. (Wash. D. C.)* **2020**, 1934848 (2020).
42. Liu, Z. et al. Maximizing the performance of n-type Mg_3Bi_2 based materials for room-temperature power generation and thermoelectric cooling. *Nat. Commun.* **13**, 1120 (2022).
43. Condron, C. L., Kauzlarich, S. M., Gascoin, F. & Snyder, G. J. Thermoelectric properties and microstructure of Mg_3Sb_2. *J. Solid State Chem.* **179**, 2252–2257 (2006).
44. Bano, S., Chetty, R., Babu, J. & Mori, T. $Mg_3(Sb,Bi)_2$-based materials and devices rivaling bismuth telluride for thermoelectric power generation and cooling. *Device* **2**, 100408 (2024).
45. Imasato, K. et al. Metallic n-type Mg_3Sb_2 single crystals demonstrate the absence of ionized impurity scattering and enhanced thermoelectric performance. *Adv. Mater.* **32**, e1908218 (2020).
46. Ying, P. et al. A robust thermoelectric module based on MgAgSb/$Mg_3(Sb,Bi)_2$ with a conversion efficiency of 8.5% and a maximum cooling of 72 K. *Energy Environ. Sci.* **15**, 2557–2566 (2022).
47. Jin, M., Lin, S., Li, W., Zhang, X. & Pei, Y. Nearly isotropic transport properties in anisotropically structured n-type single-crystalline Mg_3Sb_2. *Mater. Today Phys.* **21**, 100508 (2021).
48. Pan, Y. et al. $Mg_3(Bi,Sb)_2$ single crystals towards high thermoelectric performance. *Energy Environ. Sci.* **13**, 1717–1724 (2020).
49. Mao, J. et al. Manipulation of ionized impurity scattering for achieving high thermoelectric performance in n-type Mg_3Sb_2-based materials. *Proc. Natl Acad. Sci. USA* **114**, 10548–10553 (2017).
50. Shuai, J. et al. Tuning the carrier scattering mechanism to effectively improve the thermoelectric properties. *Energy Enviro. Sci.* **10**, 799–807 (2017).
51. Liu, Z. et al. Demonstration of ultrahigh thermoelectric efficiency of ~7.3% in Mg_3Sb_2/MgAgSb module for low-temperature energy harvesting. *Joule* **5**, 1196–1208 (2021).
52. Yang, K. et al. Robust room temperature thermoelectric performance of $Mg_3(Sb, Bi)_2$-based alloys via multivalent Mn doping. *Adv. Funct. Mater.* **34**, 2315886 (2024).
53. Zhang, F. et al. High-performance N-type Mg_3Sb_2 towards thermoelectric application near room temperature. *Adv. Funct. Mater.* **30**, 1906143 (2019).
54. Li, J. W. et al. Wide-temperature-range thermoelectric n-type $Mg_3(Sb,Bi)_2$ with high average and peak zT values. *Nat. Commun.* **14**, 7428 (2023).
55. Chen, X. et al. Extraordinary thermoelectric performance in n-type manganese doped Mg_3Sb_2 Zintl: high band degeneracy, tuned carrier scattering mechanism and hierarchical microstructure. *Nano Energy* **52**, 246–255 (2018).
56. Wang, L. et al. High-performance Mg_3Sb_2-based thermoelectrics with reduced structural disorder and microstructure evolution. *Nat. Commun.* **15**, 6800 (2024).
57. Xiong, C. et al. Achieving high thermoelectric performance of n-type $Bi_2Te_{2.79}Se_{0.21}$ sintered materials by hot-stacked deformation. *ACS Appl. Mater. Interfaces* **13**, 15429–15436 (2021).
58. Xiao, Y. et al. High-ranged ZT value promotes thermoelectric cooling and power generation in n-type PbTe. *Adv. Energy Mater.* **12**, 2200204 (2022).
59. Deng, Q. et al. Lattice defect engineering advances n-type PbSe thermoelectrics. *Nat. Commun.* **16**, 656 (2025).
60. Cheng, K. et al. Efficient $Mg_2Si_{0.3}Sn_{0.7}$ thermoelectrics demonstrated for recovering heat of about 600. *K. Mater. Today Phys.* **28**, 100887 (2022).
61. Su, L. et al. High thermoelectric performance realized through manipulating layered phonon-electron decoupling. *Science* **375**, 1385–1389 (2022).
62. Yu, J. et al. Half-Heusler thermoelectric module with high conversion efficiency and high power density. *Adv. Energy Mater.* **10**, 2000888 (2020).
63. Hu, Y. et al. Stepwise optimization of thermoelectric performance in n-type SnS. *Adv. Funct. Mater.* **35**, 2414881 (2024).
64. Meng, K. et al. Thermoelectric properties of n-type SiGe alloys with Sn incorporation. *Rare Met.* **41**, 4156–4163 (2022).
65. Li, D. et al. Fast fabrication of high-performance $CoSb_3$-based thermoelectric Skutterudites via one-step Yb-promoted peritectic solidification. *Adv. Funct. Mater.* **33**, 2305269 (2023).
66. Deng, R. et al. High thermoelectric performance in $Bi_{0.46}Sb_{1.54}Te_3$ nanostructured with ZnTe. *Energy Environ. Sci.* **11**, 1520–1535 (2018).
67. Jiang, Y. et al. Evolution of defect structures leading to high ZT in GeTe-based thermoelectric materials. *Nat. Commun.* **13**, 6087 (2022).
68. Qin, Y. et al. Grid-plainification enables medium-temperature PbSe thermoelectrics to cool better than Bi_2Te_3. *Science* **383**, 1204–1209 (2024).
69. Hao, F. et al. High efficiency Bi_2Te_3-based materials and devices for thermoelectric power generation between 100 and 300 °C. *Energy Environ. Sci.* **9**, 3120–3127 (2016).
70. Zhu, Y. K. et al. Mediating point defects endows n-type Bi_2Te_3 with high thermoelectric performance and superior mechanical robustness for power generation application. *Small* **18**, e2201352 (2022).
71. Zhu, B. et al. Realizing record high performance in n-type Bi_2Te_3-based thermoelectric materials. *Energy Environ. Sci.* **13**, 2106–2114 (2020).
72. Kim, H.-S., Gibbs, Z. M., Tang, Y., Wang, H. & Snyder, G. J. Characterization of Lorenz number with Seebeck coefficient measurement. *APL Mater.* **3**, 041506 (2015).
73. Agne, M. T., Hanus, R. & Snyder, G. J. Minimum thermal conductivity in the context of diffuson-mediated thermal transport. *Energy Environ. Sci.* **11**, 609–616 (2018).
74. Heremans, J. P. The anharmonicity blacksmith. *Nat. Phys.* **11**, 990–991 (2015).
75. Ghasemi Hajiabadi, M., Zamanian, M. & Souri, D. Williamson–Hall analysis in evaluation of lattice strain and the density of lattice dislocation for nanometer scaled ZnSe and ZnSe:Cu particles. *Ceram. Int.* **45**, 14084–14089 (2019).
76. Callaway, J. Model for lattice thermal conductivity at low temperatures. *Phys. Rev.* **113**, 1046–1051 (1959).
77. Chen, Z. et al. Vacancy-induced dislocations within grains for high-performance PbSe thermoelectrics. *Nat. Commun.* **8**, 13828 (2017).
78. Wang, L. et al. Realizing high thermoelectric performance in N-Type $Mg_3(Sb, Bi)_2$-based materials via synergetic Mo addition and Sb–Bi ratio refining. *Adv. Energy Mater.* **13**, 2301667 (2023).
79. Lei, J. et al. Approaching crystal's limit of thermoelectrics by nano-sintering-aid at grain boundaries. *Nat. Commun.* **15**, 6588 (2024).
80. Lu, Y. et al. Staggered-layer-boosted flexible Bi_2Te_3 films with high thermoelectric performance. *Nat. Nanotechnol.* **18**, 1281–1288 (2023).
81. Zhou, Y. et al. Physics-guided co-designing flexible thermoelectrics with techno-economic sustainability for low-grade heat harvesting. *Sci. Adv.* **9**, eadf5701 (2023).
82. Mao, D. et al. Scalable and sustainable manufacturing of twin boundary-enhanced flexible $Bi_{0.4}Sb_{1.6}Te_3$ films with high thermoelectric performance. *Joule* **8**, 3313–3323 (2024).
83. Wu, X. et al. Interface and surface engineering realized high efficiency of 13% and improved thermal stability in $Mg_3Sb_{1.5}Bi_{0.5}$-based thermoelectric generation devices. *Adv. Energy Mater.* **12**, 2203039 (2022).

84. Yin, L. et al. Reliable N-type $Mg_{3.2}Sb_{1.5}Bi_{0.49}Te_{0.01}$/304 stainless steel junction for thermoelectric applications. *Acta Mater.* **198**, 25–34 (2020).
85. Li, J. W. et al. Bi-deficiency leading to high-performance in $Mg_3(Sb,Bi)_2$-based thermoelectric materials. *Adv. Mater.* **35**, e2209119 (2023).
86. Shang, H. et al. N-type Mg_3Sb_2-Bi with improved thermal stability for thermoelectric power generation. *Acta Mater.* **201**, 572–579 (2020).
87. Zhu, Q., Song, S., Zhu, H. & Ren, Z. Realizing high conversion efficiency of Mg_3Sb_2-based thermoelectric materials. *J. Power Sources* **414**, 393–400 (2019).
88. Xu, C. et al. Scalable synthesis of n-type $Mg_3Sb_{2-x}Bi_x$ for thermoelectric applications. *Mater. Today Phys.* **17**, 100336 (2021).
89. Agne, M. T. et al. Heat capacity of Mg_3Sb_2, Mg_3Bi_2, and their alloys at high temperature. *Mater. Today Phys.* **6**, 83–88 (2018).
90. Chetty, R., Babu, J. & Mori, T. Best practices for evaluating the performance of thermoelectric devices. *Joule* **8**, 556–562 (2024).

Acknowledgements

This work was supported by JST Mirai Program (JPMJMI19A1, T. M.)

Author contributions

G.W. and T. M. designed this work. G.W. synthesized the sample, tested the transport properties, did the data curation, and wrote this manuscript. A.L. provided the MgAgSb sample. L.W. investigated the PPMS test. X.W. (Xinzhi Wu) and X.W. (Xinyuan Wang) played a part in the discussion. T.M. provided supervision and the funding. All authors have reviewed and approved the final version of the manuscript.

Competing interests

The authors declare no competing interests.

Additional information

Supplementary information The online version contains supplementary material available at https://doi.org/10.1038/s41467-025-65325-7.

Correspondence and requests for materials should be addressed to Takao Mori.

Peer review information *Nature Communications* thanks Hanfu Wang and the other anonymous reviewer(s) for their contribution to the peer review of this work. A peer review file is available.